Indirect Effects of Binary Typhoons on an Extreme Rainfall Event in Henan Province, China From 19 to 21 July 2021. 3. Sensitivities to Microphysics Schemes

Hongxiong Xu[1] , Dajun Zhao[1] , Jinfang Yin[1], Yihong Duan[1] , Wenhua Gao[1], Ying Li[2] , and Linli Zhou[3,4]

[1]State Key Laboratory of Severe Weather, Chinese Academy of Meteorological Sciences, China Meteorological Administration, Beijing, China, [2]Laboratory for Climate Studies, National Climate Center, China Meteorological Administration, Beijing, China, [3]Zhejiang Province Meteorological Observatory, Zhejiang, China, [4]Zhejiang Institute of Meteorological Sciences, Zhejiang, China

Abstract Previous numerical studies have focused on the direct impact of microphysics schemes on multiscale atmospheric systems that produce rainfall. However, the indirect impact of microphysics schemes on the key large-scale circulation around areas of extreme rainfall has not yet been examined systematically. We used the ARW-WRF (Advanced Research WRF (Weather Research and Forecasting) Model) to simulate the extreme rainfall event in Henan province, China from 19 to 21 July 2021. Experiments were conducted to investigate the sensitivity of the simulation to the three popular double-moment microphysics parameterizations: the Thompson, Morrison and WDM6 (WRF Double-Moment 6-Class Microphysics Schemes). We found significant sensitivity to the microphysics parameterization, with the maximum precipitation varying by up to 400 mm and the area-averaged precipitation by 33 mm. The Thompson and Morrison microphysics schemes produced the largest amount of precipitation, whereas the WDM6 scheme produced the smallest amount of precipitation. The simulated southerly flow varied substantially between the different microphysics schemes. This is due to the ability of the microphysics schemes to produce latent heat, which enhances the southerly flow, leading to more intense precipitation. The higher the parameterized latent heat, the stronger and more obvious the southerly flow over southern Henan province, with the WDM6 scheme simulating a much weaker southerly flow and the Thompson scheme producing the strongest southerly flow. These results indicate that the indirect effects on the key circulation patterns can be just as sensitive to the formulation of the microphysics scheme as the direct effects on extreme rainfall. These results may help to improve the prediction of extreme rainfall events.

Plain Language Summary Complex microphysical processes have crucial impacts on the accurate prediction of the intensity and areal extent of extreme rainfall. However, previous studies have focused on rain amount related to the microphysical schemes caused by intrinsic microphysical processes or direct influencing systems—such as typhoons, squall lines and convective systems—and little attention has been paid to increase of rain amount related to the microphysical schemes caused by the surrounding key circulation of extreme rainfall. Through numerical simulations of the extreme rainfall event in Henan province, China from 19 to 21 July 2021 using three popular microphysics schemes, we show that indirect effect of microphysical schemes on the extreme rainfall can effectively regulate the southerly flow over southern China. The microphysics schemes influence the southerly flow through latent heating. A greater amount of latent heat can produce a stronger southerly flow, which favors the transport of water vapor and energy to the Henan region and produce more intense precipitation.

1. Introduction

It is well known that complex microphysical processes determine the characteristics of cloud particle populations as a response to the resolved atmospheric motion and as feedback to the atmospheric environment via the action of individual cloud particles (Bao et al., 2019; Khain et al., 2015). Thus, microphysical processes are crucial in the accurate prediction of the intensity and areal extent of rainfall because they have important roles in the phase changes of water and the transfer of thermal energy (Ferrier et al., 1995; Gao et al., 2021; Xue et al., 2017). However, the representation of microphysical processes is still uncertain, even with state-of-the-art microphysics

schemes in numerical models and especially under extreme rainfall conditions (Morrison et al., 2020). The accurate representation and evaluation of microphysical processes in current numerical weather prediction is therefore both a major concern of operational modelers (Dowell et al., 2022; Zhang, 2019; Zhou et al., 2019) and a challenge for researchers (Chen et al., 2021; Gao et al., 2021; Kreidenweis et al., 2019; Tapiador et al., 2019).

In general, microphysics schemes can be divided into bin and bulk schemes. Bulk schemes are currently more suitable for numerical simulations than bin schemes because less computing power is required (Lei et al., 2020). Many studies have suggested that the use of different schemes can have large effects on the simulated cloud and convective systems. For example, Huang et al. (2020) compared the performance of three microphysics schemes in simulating a coastal extreme rainfall event and concluded that the simulated precipitation in the WSM6 single-moment scheme outperformed the Thompson and Morrison double-moment schemes in terms of intensity and coverage compared with the observations. Thomas et al. (2021) suggested that the Thompson aerosol awareness scheme reasonably reproduced the spatial and temporal distribution of observed precipitation over Kerala in southwest India, whereas the WSM6 scheme largely underestimated the intensity of rainfall in the mountains throughout the precipitation event. It is unclear whether the differences in these simulations were a result of the different basic construction of the schemes or whether they were a result of the different assumptions made by these schemes when parameterizing the same process (Falk et al., 2019).

Many of the microphysical processes in multi-moment schemes have been shown to have promising applications in numerical weather forecasting models. For example, Bryan and Morrison (2012) demonstrated the superior performance of the double-moment scheme over the single-moment scheme by investigating an idealized squall line simulation. However, the large discrepancy in the results simulated by the Morrison and Milbrandt and Yau (M-Y schemes) suggests that uncertainties remain even when using the double-moment scheme. Lim and Hong (2010) developed a WDM6 (WRF Double-Moment 6-Class Microphysics Scheme) based on the WSM6 single-moment scheme and showed that the former outperformed the latter in both simulations of a 2D ideal and a 3D real event as a result of the increased number of concentration predictions (Hong & Lim, 2006; Lim & Hong, 2010). Luo et al. (2018) used multi-moment microphysics schemes to reproduce a hailstorm event and concluded that the multi-moment scheme could simulate more realistic hail structures than the single-moment scheme.

Although the microphysics scheme has a crucial role in the development and structure of extreme rainfall events, recent improvements in microphysics observations and our understanding of microphysical processes have not yet been fully reflected in improved numerical models (Halder et al., 2015), leading to considerable uncertainties remaining in microphysical parameterization (Bao et al., 2019). Thus, regardless of the complexity, the uncertainties associated with microphysical parameterizations remain large in current numerical weather prediction models, leading to considerable variations in the distribution and intensity of simulated extreme rainfall events in high resolution mesoscale numerical models among different microphysics schemes (Morrison & Milbrandt, 2011). Thus, it is difficult to determine which microphysics scheme is suitable for simulation based on the degree of complexity. We therefore need to conduct more intercomparison and sensitivity research between different microphysics parameterizations to investigate the dominant factors resulting in different simulations of individual events (Huang et al., 2020).

More importantly, the correct representation of microphysics processes is essential in numerical models because cloud-related latent heat drives the atmospheric circulation (Wang et al., 2021). Continuous efforts have been made to examine the sensitivity of the simulated meteorological phenomena at widely varying scales—such as squall lines (Huang et al., 2020; Xue et al., 2017), tropical cyclones (Wang, 2009; Zhao et al., 2020) and extreme rainfall events—to different microphysics schemes. For example, changes in the microphysics that influence the latent cooling of clouds induce differences in cold pools and thus the dynamics through the mechanisms outlined in the Rotunno–Klemp–Weisman theory (Morrison & Milbrandt, 2011). Direct changes in heating and cooling through microphysical processes or indirect changes in latent heating and cooling through aerosols can significantly affect the intensity, structure, size and rainbands of tropical cyclones (Wang et al., 2009). Uncertainties in cloud microphysical processes may also lead to large biases in the multiscale circulation and result in significant differences in precipitation and storms through this feedback. However, most previous research has focused on increase of rain amount related to the microphysical schemes caused by intrinsic microphysical processes or direct influencing systems such as typhoons, squall lines and convective systems. While little attention has been paid to increase of rain amount related to the microphysical schemes caused by the surrounding key circulation

of the target weather systems. Hereafter, increase of rain amount caused by intrinsic microphysical processes and direct/local influencing systems related to the microphysical schemes is referred to as direct/local effect of microphysics, while increase of rain amount caused by the surrounding/nonlocal key circulation related to the microphysical schemes is referred to as indirect/nonlocal effect of microphysics.

The Henan extreme rainfall event from 19 to 21 July 2021 was the second largest precipitation event in the Henan region since meteorological records began. The maximum hourly rainfall in Zhengzhou, the provincial capital, reached 201.9 mm. The event resulted in more than 300 casualties and large amounts of damage to properties (Chen et al., 2022; Yin et al., 2022) and attracted widespread attention from researchers (Fu et al., 2022; Nie & Sun, 2022). The ensemble-based analysis and numerical simulations in the previous two parts of this study (Xu, Duan, Li, et al., 2022; Xu, Duan, Xu, 2022) suggested that the southerly flow had a key role in the water vapor, energy, and the intensity and location of the convergence zone in the Henan region, and also significantly affected the intensity of precipitation. The interaction of typhoons In-fa (2021) and Cempaka (2021) affected the southerly flow and indirectly influenced the extreme rainfall. Thus, the extreme rainfall event is an ideal candidate for investigating the indirect effects of microphysics processes because the southerly flow had a crucial role in the area of heavy rainfall and was sensitive to the microphysics parameterization, allowing further investigation of the mechanisms.

Based on the previous studies analyzed above, the current study attempts (for the first time in the literature) to investigate the indirect impact of three popular microphysics schemes in the Weather Research and Forecasting (WRF) model during the extreme rainfall event in Henan province, China from 19 to 21 July 2021. The goal of this study was to extend the simulation conducted in Part 2 using different microphysics schemes to advance our understanding on the indirect effects of the differences in microphysical processes between these schemes on the evolution of an extreme rainfall event. Specifically, we address the following questions: (a) can microphysical processes influence the southerly flow and then affect the extreme rainfall; and (b) what are the effects of microphysical processes on the southerly flow in the region of extreme rainfall and what are the underlying physical processes?

The remaining sections of this paper are organized as follows. Section 2 describes the experimental design. Section 3 compares the extreme rainfall and southerly flow. Sections 4 and 5 provide a detailed analysis of the hydrometeors and thermodynamic differences, respectively. The momentum and thermal budget is analyzed in Section 6 and Section 7 gives our discussion and conclusions.

2. Model Configuration and Experimental Design

We used Version 4.2.1 of the Advanced Research WRF (WRF-ARW) model to simulate this record-breaking rainfall event in Henan. Identical to the method of Xu, Duan, Li, et al. (2022), the model was initialized at 0000 UTC on 18 July 2021 and integrated forward for 72 hr. The model physics used during this time were the Mellor–Yamada–Nakanishi–Niino planetary boundary layer and surface layer scheme (Nakanishi & Niino, 2006; Olson et al., 2019; Siebesma et al., 2007). The model was configured as two-way nested meshes with horizontal grid spacings of 12 and 3 km, and grid size of 652×463 and 345×385, respectively. There are 50 stretched vertical layers, extending from the surface to 50 hPa. Due to the large area involved in the indirect effects of microphysical processes, 12-km model data at 1-hr intervals are used for the analysis in this study. More details on the relevant model configurations can be found in Xu, Duan, Li, et al. (2022). We examined three double-moment microphysics schemes. In Part 2, the model simulation with the Thompson microphysics scheme (Thompson & Eidhammer, 2014) simulated the extreme rainfall event reasonably well in terms of the key weather circulation patterns (e.g., the southerly and southeasterly flows and the location of the two typhoons) and the intensity of rainfall. Hereafter, the original simulation with the Thompson scheme is referred to as the Thompson experiment.

To further analyze the effect of the microphysics scheme on this extreme precipitation event, we conducted two additional experiments with the same settings as the Thompson experiment, but with the microphysical schemes replaced by the Morrison (Morrison et al., 2009) and WDM6 (Lim & Hong, 2010) schemes. The simulations using the Morrison and WDM6 schemes are hereafter referred to as the Morrison and WDM6 experiments, respectively. For the mass mixing ratios, all the schemes predict five features of clouds: cloud water (QCLOUD), rainwater (QRAIN), cloud ice (QICE), snow (QSNOW) and graupel (QGRAUPEL). For the particle number of hydrometeors, the Thompson scheme predicts the number concentrations of rainwater and cloud ice, the WDM6
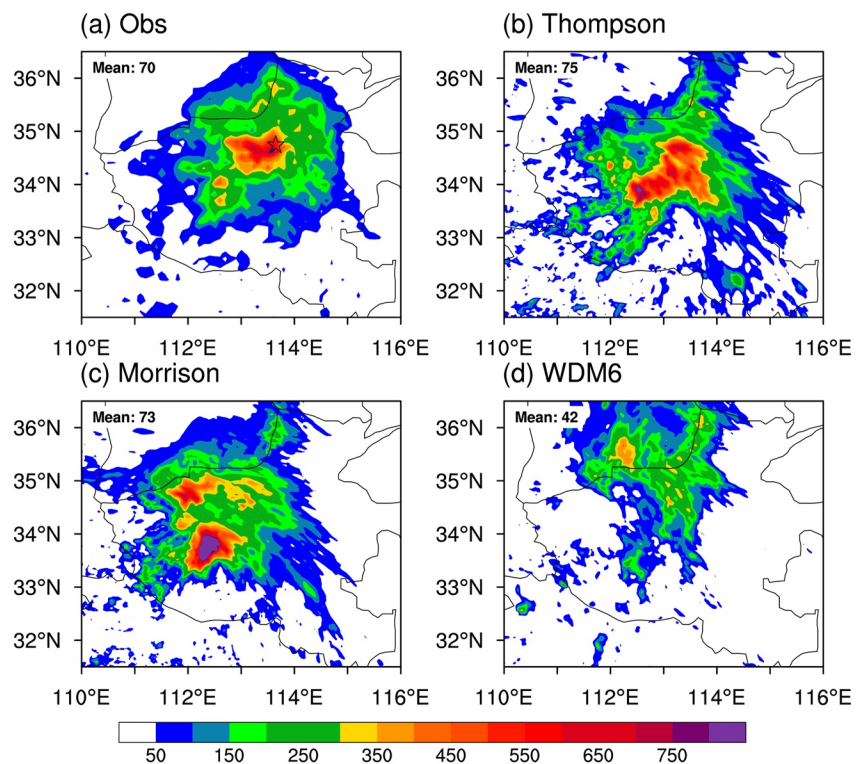
Figure 1. 48-hr accumulated precipitation (mm) between 0000 UTC on 19 July and 0000 UTC on 21 July 2021 for the (a) China Meteorological Administration observations and the (b) Thompson, (c) Morrison and (d) WDM6 experiments. The black star represents location of Zhengzhou city.

scheme predicts the number concentrations of cloud, rain and cloud condensation nuclei, whereas the Morrison microphysics scheme predicts the number concentration of all the hydrometeors except cloud water. The following sections compare the three microphysics schemes and discuss the indirect effects of the microphysics schemes on the prediction of extreme rainfall and the southerly flow.

3. Extreme Rainfall and the Southerly Flow

We compared the horizontal distribution of the simulated rainfall from 0000 UTC on 19 July to 0000 UTC on 21 July 2022 with the China Meteorological Administration (CMA) merged rainfall data set to investigate the impact of the different microphysics schemes on modeling the accumulated precipitation (Figure 1a). The observed accumulated rainfall clearly shows torrential rainfall between 19 and 21 July, mainly over central and northern Henan province. The simulated distribution of the 48-hr accumulated precipitation shows substantial differences among the microphysics schemes. The area-averaged precipitation over the Henan region in the Thompson (75 mm; Figure 1b) and Morrison (73 mm; Figure 1c) experiments is close to the observations (70 mm; Figure 1a), but is lower in the WDM6 experiment (42 mm; Figure 1d). The overestimation of the area-averaged precipitation is mainly due to the overestimation of heavy precipitation in southwest Henan by the Thompson and Morrison schemes. The observed spatial pattern is reasonably well reproduced in the Thompson experiment, followed by the Morrison experiment, despite the overestimation in southwest Henan.

Different from the area-averaged precipitation, the model-simulated intensity and location of precipitation near Zhengzhou is closest to the observations in the Thompson experiment (Figure 1b). The Morrison experiment (Figure 1c) produces a precipitation pattern similar to the Thompson experiment, but the area of heavy precipitation near Zhengzhou is smaller and sparser and the heavy precipitation southwest of Henan extends more to the southwest with a stronger intensity. The most extreme amounts of rainfall in the Morrison run are located in southwestern Henan, in contrast with the observed location near Zhengzhou. Although the WDM6 (Figure 1d) scheme also simulated heavy rainfall over northern Henan, the maximum precipitation is about 400 mm less and
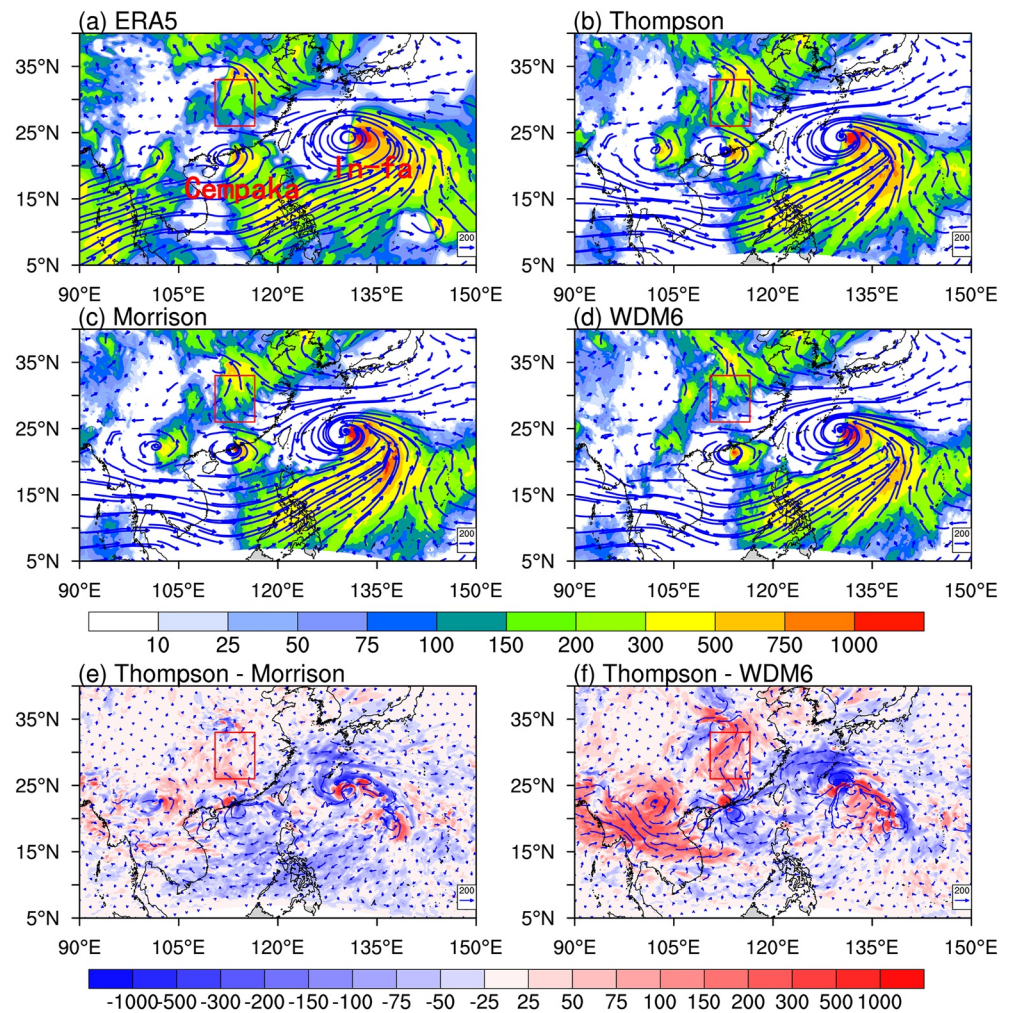
Figure 2. Column-integrated moisture flux (vectors) and its meridional magnitude (shading; kg m^{-2} s^{-1}) for (a) the ERA5 data set and the (b) Thompson, (c) Morrison and (d) WDM6 experiments at 0000 UTC on 20 July 2021. Difference in the column-integrated moisture flux and its magnitude at 0000 UTC on 20 July 2021 between (d) the Thompson and Morrison experiments and (e) the Thompson and WDM6 experiments. The red rectangles indicate the location of the southerly flow.

the area of heavy rainfall is significantly smaller than in the other two schemes. In addition, the northern edge of accumulated precipitation extends further north in the WDM6 experiment than in the Morrison and Thompson experiments, indicating that the WDM6 scheme is unable to simulate the observed precipitation intensity and center of heavy precipitation. In general, the variation in the structure of horizontal precipitation between the different microphysics schemes indicates that the quantitative prediction of precipitation is highly dependent on the accurate representation of the cloud microphysics.

The column-integrated moisture flux is a good measure of whether the transported moisture contributed to the precipitation (Wang et al., 2009) in the different microphysics schemes. Figures 2a–2d shows examples of the column-integrated moisture flux at 0000 UTC on 20 July 2021—that is, at the time before the observed maximum precipitation from the ERA5 (The fifth generation of the European Centre for Medium-Range Weather Forecasts (ECMWF) Re-Analysis (ERA)) reanalysis data set and the simulations. In the ERA5 reanalysis data set (Figure 2a), the two flows of moisture to the Henan region are adjacent to two typhoons over the Northwest Pacific and the South China Sea. A strong southeasterly flow transported to Henan along the edge of subtropical high. A strong southerly flow is detected over south of Henan, stretching from southern China to Henan province. The southerly column moisture flux of the southerly flow is confined to a narrow region between 110.5°E and 116.5°E.

As shown in Xu, Duan, Li, et al. (2022) and Xu, Duan, Xu (2022), the rainfall in the Henan region was closely related to two moisture flow from the south and southeast. These important features in the ERA5 reanalysis data

set were reasonably reproduced in all three microphysics schemes, where there were two distinct channels of water vapor moving toward Henan province, mainly distributed in the southeasterly flow from eastern China and the southerly flow from southern China. Specifically, the main features of this southeasterly flow are well simulated by all three microphysics schemes, including the location and amplitudes the southeasterly flow. However, the amplitude of simulated southerly flow north of typhoon Cempaka shows substantial differences among the microphysics schemes.

The southerly flow (indicated by the meridional column-integrated moisture flux) extends more southward in the Thompson and Morrison experiments than in the WDM6 experiment, indicating that a weaker southerly flow is produced in the WDM6 experiment. This corresponds to the clearly smaller and sparser coverage of the area of accumulated precipitation in the WDM6 experiment. Consistent with the precipitation shown in Figure 1, the southerly flow of the column-integrated moisture flux is much weaker in the WDM6 experiment than in the other two experiments, suggesting that the microphysics schemes not only contributed to the southerly flow, but also to the intensity, location and region of precipitation in the Henan region and the adjacent seas. This confirms that the southerly flow has an important influence on the intensity and distribution of extreme rainfall, consistent with the first two parts of this study (Xu, Duan, Li, et al., 2022; Xu, Duan, Xu, 2022).

To further examine the differences in the column-integrated moisture flux among the schemes in more detail, Figures 2e and 2f show the differences in the column-integrated moisture flux and its magnitude at 0000 UTC on 20 July 2021 between the Thompson experiment and the Morrison and WDM6 experiments, respectively. The magnitude of column-integrated moisture flux over southerly flow region is about 200 kg m^{-2} s^{-1} smaller in the WDM6 experiment (Figure 2f), coinciding with the weaker precipitation, but is only marginally smaller in the Morrison experiment (<75 kg m^{-2} s^{-1}; Figure 2e) than in the Thompson experiment. Another notable feature is that the mesoscale vortex near Henan is more intense in the Thompson and Morrison experiments, but weaker in the WDM6 experiment, compared with that in the ERA5 reanalysis data set. This indicates that the intensity of the mesoscale vortex is associated with the increase in the stronger southerly flow. However, the differences in the southeasterly flow between the different microphysics schemes is less evident, suggesting an insignificant effect of the microphysics schemes on the southeasterly flow. This analysis indicates that the variation in the microphysics schemes may have an important influence on the southerly flow. The difference in the southerly flow between the WDM6 and Thompson experiments is comparable with the magnitude of the effect produced by the interaction of the binary typhoons described in Part 2 of this series of papers. So the question arises, how do microphysical processes affect the southerly flow? The following sections analyze the impact of microphysical processes over the region of southerly flow based on these results.

4. Differences in the Hydrometeors

We started with an investigation of the hydrometeors in each experiment to work toward an understanding of how the microphysics schemes contribute to or inhibit the southerly flow. The time history of the hydrometeors during the rainfall event was investigated using the time–height vertical cross-sections up to 14 km of QCLOUD, QRAIN, QGRAUPEL, QSNOW, and QICE from 0000 UTC on 18 July to 0000 UTC on 21 July averaged over the region of southerly flow (Figure 2, red box). The cloud and rain mixing ratio in the Morrison (Figures 3b and 3e) and Thompson (Figures 3c and 3f) experiments are qualitatively similar, with each scheme showing clear diurnal variations throughout the simulation. The cloud mixing ratio in both experiments shows a maximum of roughly the same magnitude below 2 km in the southerly flow region. The Morrison scheme produces slightly higher values above 2 km for the first 12 hr of the simulation. Although the initial value of the cloud rain mixing ratio was zero in all three experiments, it increased rapidly during the model integration, with the WDM6 experiment (Figure 3c) producing the highest cloud mixing ratio in the three experiments. For example, the maximum cloud mixing ratio during the last 24 hr of the Morrison and Thompson simulations was about 2.0×10^{-5} kg kg^{-1} (Figures 3a and 3b), whereas it reached 10.0×10^{-5} kg kg^{-1} in the WDM6 experiment (Figure 3c).

The rain mixing ratio for all the experiments shows a higher value below 5 km in the southerly flow region and clear diurnal variations during the rainfall event. However, the rain mixing ratio in the WDM6 experiment (Figure 3f) differs significantly from those in the Morrison (Figure 3e) and Thompson (Figure 3d) experiments. Although the WDM6 run also produces a strong rain mixing ratio (Figure 3f) for the first 24 hr from the surface to about 5 km. After an initial gestation period, a period of rapidly decreasing rain is observed starting at about 24 hr for the WDM6 experiment (Figure 3f) and continuing almost up to the end of the simulation. During this time, the
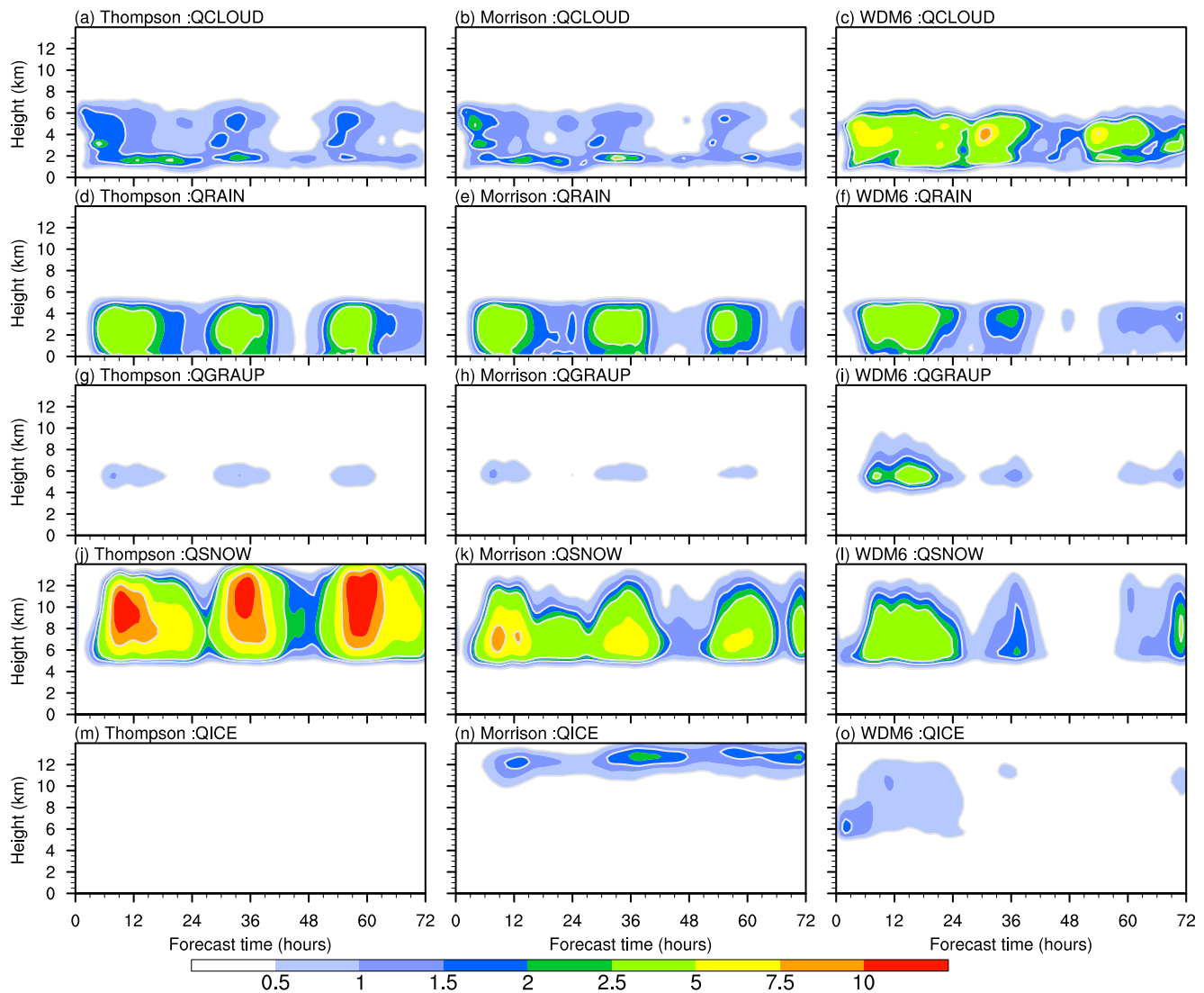
Figure 3. Time–height sections of (a–c) QCLOUD, (d–f) QRAIN, (g–i) QGRAUPEL, (j–l) QSNOW and (m–o) QICE averaged over the area of southerly flow (Figure 2a; red box) for (a, d, g, j, m) the Thompson experiment, (b, e, h, k, n) the Morrison experiment and (c, f, i, l, o) the WDM6 experiment (units: 10^{-5} kg kg^{-1}).

maximum rain mixing ratio is reduced to about 2.0×10^{-5} kg kg^{-1} at 36 hr and 1.0×10^{-5} kg kg^{-1} at 72 hr. The rain mixing ratio at the end of the simulation is seven times less than in the Morrison and Thompson experiments. Clearly, the WDM6 scheme produces the largest cloud mixing ratio and the smallest rain mixing ratio. Although the cloud mixing ratio in Figure 3c reaches a quasi-steady state, the rain mixing wind continues to decrease. These lower values of the rain mixing ratios in the WDM6 experiment, which extend the surface to about 5 km compared with the other two experiments, may be produced in association with the cloud mixing ratio.

The magnitude and vertical distribution of ice-phase hydrometeors in the Thompson and Morrison experiments differ markedly from those in the WDM6 experiment. The QSNOW hydrometeors are mainly located from the upper mid-troposphere to about 14 km in the Thompson experiment (Figure 3g), 13 km in the Morrison experiment (Figure 3h) and about 12 km in the WDM6 experiment (Figure 3i). The Morrison experiment simulates a greater amount of cloud ice from 11 to 14 km, whereas the WDM6 experiment produces a greater amount of cloud ice from 5 to 12 km. Noticeably, the Morrison (Figure 3k) and Thompson (Figure 3j) experiments simulate a greater amount of cloud snow than the WDM6 experiment (Figure 3l), although the cloud water mixing ratio is much less than in the WDM6 experiment. For example, the peak QSNOW can be greater than 10×10^{-5} kg kg^{-1} in the Thompson run (Figure 3j) and about 10×10^{-5} kg kg^{-1} in the Morrison run (Figure 3k), but about 5×10^{-5} kg kg^{-1} in the WDM6 run (Figure 3l) in the first 24 hr of simulation. Interestingly, in the

Thompson experiment, although the snow mixing ratio is larger (Figure 3j), the ice mixing ratio (Figure 3m) is much lower than in the Morrison (Figure 3n) and WDM6 (Figure 3o) experiments. This could be a result of the stricter criteria for ice formation in the Thompson scheme (temperature < 253.15 K and supersaturation > 0.25%) than in the WDM6 scheme (temperature < 273.15 K and supersaturation > 0). Consistent with the cloud liquid water, QGRAUPEL decreases significantly in the WDM6 run (Figure 3i), but there is only a marginal change in the Morrison (Figure 3h) and Thompson (Figure 3g) experiments. For example, the maximum graupel decreases by >5 × 10^{-5} kg kg^{-1}, whereas the peak of ice decreases from 1.5 × 10^{-5} to <0.5 × 10^{-5} kg kg^{-1} in the WDM6 experiment (Figure 3i).

In summary, the area-averaged cloud and rain mixing ratio in the Morrison and Thompson experiments are generally fairly similar, except for a slightly higher rain mixing ratio in the Thompson experiment. However, the WDM6 experiment differs significantly in several ways: the rain mixing ratio is deeper and lower after 24 hr of model integration, the cloud mixing ratio is significantly larger and the maximum height is significantly higher than in the other two experiments. Both the Thompson and Morrison experiments simulate a higher amount of rain, but lower cloud water than the WDM6 experiment. The Thompson experiment simulates higher amounts of snow, whereas the Morrison experiment produces strong values for ice in the upper troposphere from 11 to 14 km. There is a significant daily variation in all the hydrometeors in the different microphysics schemes. In the Thompson and Morrison schemes, the amount of hydrometeors does not change significantly, or only decreases slightly, with the diurnal cycle of model integration, but, in the WDM6 scheme, there is a significant decrease in the amount of all hydrometeors, except for cloud water.

5. Thermodynamic Differences

The latent heat relating to cloud microphysics in the total diabatic heating of clouds is usually thought to be a crucial driver of large-scale systems (Halder et al., 2015; Huang et al., 2020). Differences in the microphysical processes among microphysics schemes may lead to substantial differences in latent heat, leading to differences in the southerly flow. This section therefore examines the differences in latent heat among the three microphysics schemes. The evolution of latent heat for each microphysical schemes was output directly from the WRF model at 1-hr intervals.

Figure 4 shows time–height sections of latent heating due to microphysics parameterization for each experiment. In general, the total latent heating due to microphysics parameterization (TTEND_MP) is largest in the Thompson experiment (Figure 4a), slightly lower in the Morrison experiment (Figure 4b) and significantly lower in the WDM6 experiment (Figure 4c). Consistent with the evolution of the hydrometeors, all the schemes also show a diurnal cycle and produce a maximum in latent heating around mid-afternoon (about 0600 UTC) over the southerly flow region. The total latent heating from the microphysics parameterizations from all three experiments shows two vertical maxima at about 4 and 7 km above the ground, but with different magnitudes (Figures 4a–4c). A continuous decrease in latent heating is observed in the WDM6 and Morrison experiments, but the magnitude of the decrease is much greater in the WDM6 experiment than in the Morrison experiment. For instance, at $t = 6$ hr, the total latent heat maximum was 11–13 × 10^{-5} K s^{-1} in the Thompson experiment and 9–11 × 10^{-5} K s^{-1} in the Morrison and WDM6 experiments. At about $t = 32$ hr, the total latent heat maximum was 9–11 × 10^{-5} K s^{-1} in the Thompson experiment, 7–9 × 10^{-5} K s^{-1} in the Morrison experiment and only 3–5 × 10^{-5} K s^{-1} in the WDM6 experiment. The fact that the magnitude of total latent heating from the Morrison experiment is much closer to that in the Thompson experiment, whereas the WDM6 experiment shows much less heating than the Thompson experiment, indicates the uncertainty of the microphysics parameterization for latent heating.

To further examine the mechanisms that result in variations in the total latent heating from microphysics parameterizations among the different microphysics experiments, the area-averaged latent heat of condensation (TTEND_COND), snow (TTEND_SNOW) and the remaining three species (rain, graupel and ice; TTEND_RES) of each scheme are shown in Figures 4d–4f, 4g–4i, and 4j–4l, respectively. The latent heat of snow is shown separately because there are significant differences in the snow mixing ratio among the three microphysics schemes. The latent heat of both condensation and snow show a diurnal cycle throughout the entire simulation period for the Thompson and Morrison experiments, consistent with the total latent heating. The area-averaged latent heat of condensation (Figures 4d–4f) is generally maximum at about 4 km, which is much closer to lower maximum center that is seen in total latent heating (Figures 4a–4c), whereas the latent heat of snow tends to peak
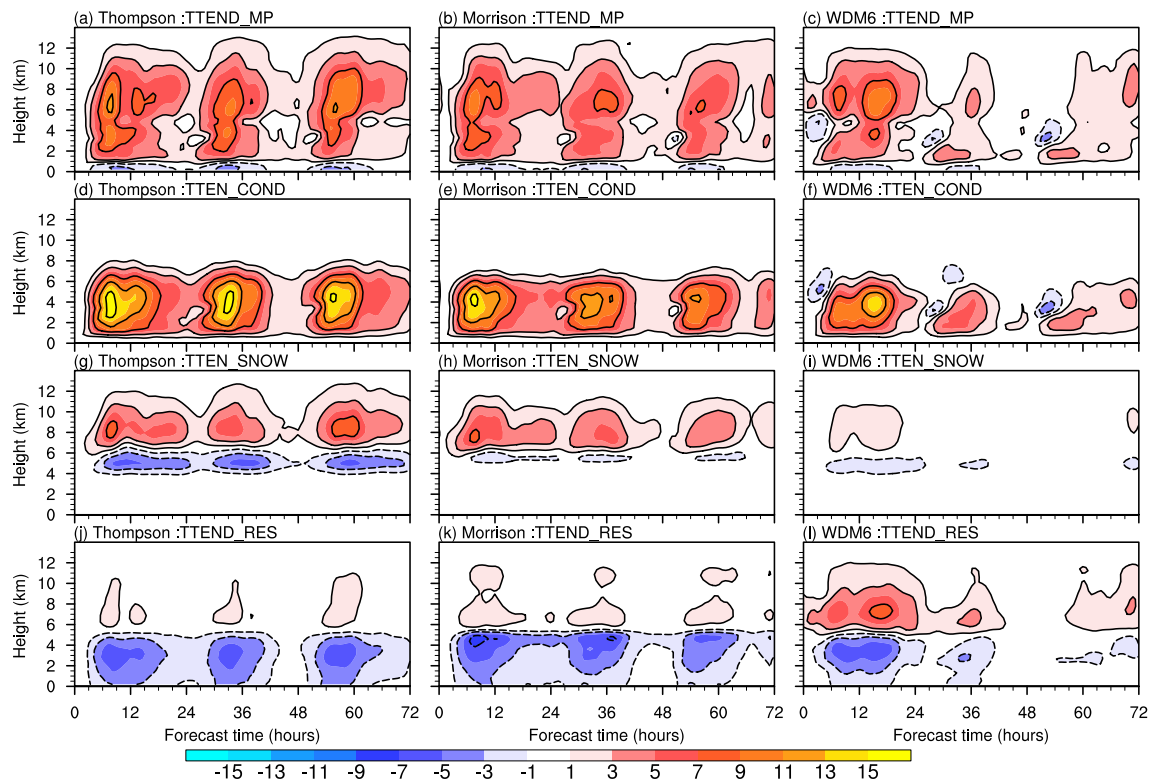
Figure 4. Time–height sections of (a–c) latent heating, (d–f) latent heat of condensation/evaporation, (g–i) latent heat of snow and (j–l) latent heat of the remaining three spices of hydrometeors (rain, graupel and ice) due to microphysics parameterization averaged over the area of southerly flow (Figure 2a; red box) for (a, d, g, j) the Thompson experiment, (b, e, h, k) the Morrison experiment and (c, f, i, l) the WDM6 experiment (units: 10^{-5} K s^{-1}).

between 8 and 10 km (Figures 4g–4i), which is higher than the upper maximum center of total latent heating resulting from the combination of condensation and snow. This may indicate that the latent heat of condensation and snow dominant the total latent heating for the two vertical maximum center, respectively. In the lower troposphere, the larger the latent heat of condensation, the larger the total latent heating, with the Thompson scheme producing the largest latent heating, followed by the Morrison and WDM6 schemes. Figure 4 clearly suggests that the weaker latent heating of the WDM6 scheme is related to the much weaker condensation. Recall that the southerly flow in the WDM6 experiment is weaker than that in the Morrison and Thompson experiments. This is consistent with the much lower total latent heating from the microphysics parameterizations. In other word, the WDM6 experiment produces much lower latent heating than the Thompson and Morrison experiments and cannot reproduce well the southerly flow during this extreme rainfall event. Previous studies showed that latent heat directly affects vertical velocity, but how it affects horizontal wind velocity (southerly airflow) remains to be further examined in the following sections.

Conceptually, a larger amount of condensation from water vapor will produce more clouds, resulting in a higher cloud mixing ratio. However, our results show that the larger amount of latent heating and cloud tendency due to condensation in the Thompson and Morrison experiments appear to contrast with the fact that the cloud mixing ratio is much less than in the WDM6 experiment. Figure 5 shows the area-averaged cloud water source (condensation), cloud water sink and the sum of auto-conversion (PRAUT) and rain collection cloud water (PRACW) to illustrate the possible reasons for the physical mechanisms of this situation. The most obvious difference between the WDM6 experiment and the Thompson and Morrison experiments is the magnitude of the cloud water tendencies in the lower troposphere. At about 4 km, both the source and sink of cloud water tendencies in the Thompson runs (Figures 5a and 5d) are twice as strong as in the WDM6 experiment (Figures 5c and 5f).

Because the modeling of extreme rainfall indicates a relationship between the total sink and rain collection for cloud water, it is instructive to compare the PRACW and PRAUT terms in each scheme. Since the PRAUT is much smaller, Figures 5g–5i clearly suggests that the total sink of cloud water (Figures 5d–5f) in all the schemes
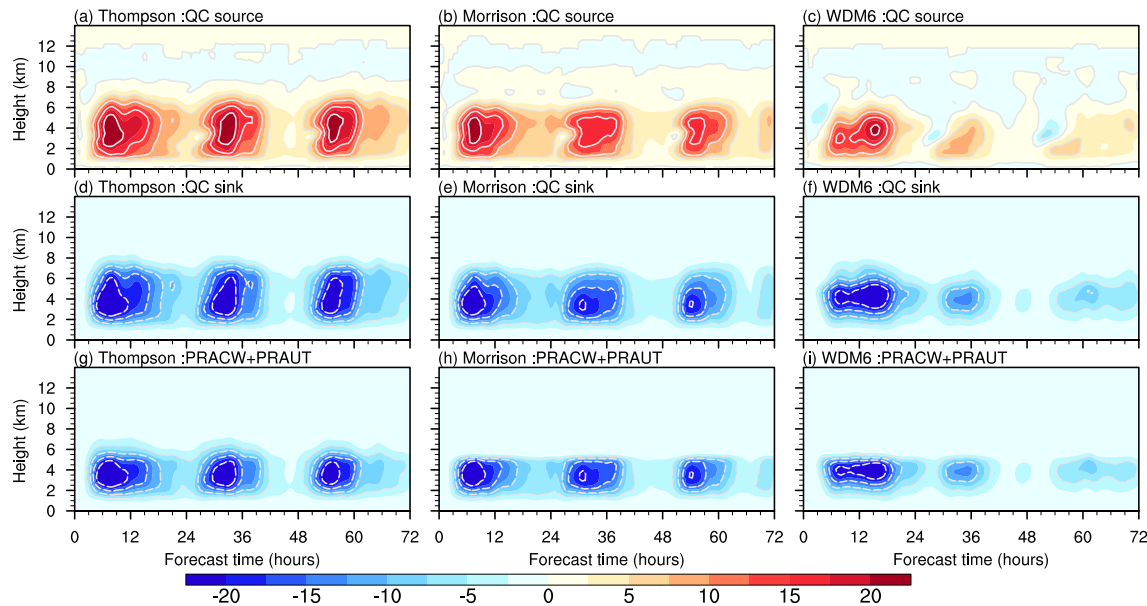
Figure 5. Time–height sections of the (a–c) QCLOUD source, (d–f) the total QCLOUD sink and (g–i) the QCLOUD sink due to auto-conversion and rain collection averaged over the area of southerly flow (Figure 2a; red box) for (a, d, g) the Thompson experiment, (b, e, h) the Morrison experiment and (c, f, i) the WDM6 experiment (units: 10^{-5} kg kg^{-1} hr^{-1}).

could be attributed to the PRACW. The question then becomes: why is the PRACW in the WDM6 experiment (Figure 5i) much smaller than that in the Thompson (Figure 5g) and Morrison (Figure 5i) experiments? The differences in cloud water could be explained by the different rain water contents: the WDM6 experiment (Figure 3f) shows much lower rain water mixing than the Thompson and Morrison experiments (Figures 3d and 3e) after 24 hr of simulation. As a result of the reduced amount of rain water in the WDM6 experiment, it is not surprising that the production of rain water due to the collection of cloud water is much lower than in the Morrison and Thompson experiments. The larger amount of cloud water in the WDM6 experiment could therefore be interpreted from the result that although source of cloud water resulted by condensation is much smaller, the smaller rain water leads to smaller rain collecting cloud water and then constrains the decrease in cloud water.

These results indicate the importance of the warm rain microphysical processes involving condensation and the collection of rain water in the Henan extreme rainfall event. The latent heat of condensation is crucial to the forecast of the southerly flow. The cloud tendencies from the collection of rain water dominate the cloud mixing ratio, which influences the latent heat of condensation and the subsequent strength of the southerly flow. Although it is not easy to examine these simulated cloud water tendencies using observations, a number of previous studies have found that both the WDM6 and WSM6 schemes underestimate the rain water mixing ratio (Huang et al., 2020; Thomas et al., 2021). Huang et al. (2020) also found that the magnitudes of latent heating and cloud tendencies in simulations of an extreme rainfall event were larger in the Thompson and Morrison schemes than in the WSM6 experiments, which agrees with the results of this study.

The latent heat associated with phase changes in water may make an important contribution to the southerly flow structure that controls many of the features of extreme rainfall. To further examine the mechanisms leading to changes in the southerly flow among the different microphysics schemes, Figures 6a and 6b show the time–height sections of the difference in potential temperature between the Morrison and WDM6 and the Thompson experiments. The difference in potential temperature between the Morrison and the WDM6 and Thompson experiments is more complex than that of latent heating. For the WDM6 experiment (Figure 6b), the potential temperature in the southerly flow region is colder in the lower troposphere, but warmer in the mid-troposphere than the potential temperature in the Thompson experiment, which may be a consequence of enhanced latent heating. The Morrison experiment (Figure 6a) shows a small difference in potential temperature in the lower troposphere and a higher potential temperature in the mid-troposphere than the WDM6 experiment. This could be because the vertical distribution of the potential temperature in the upper mid-troposphere is not only determined by latent heating, but also by other processes such as the advection of the potential temperature.
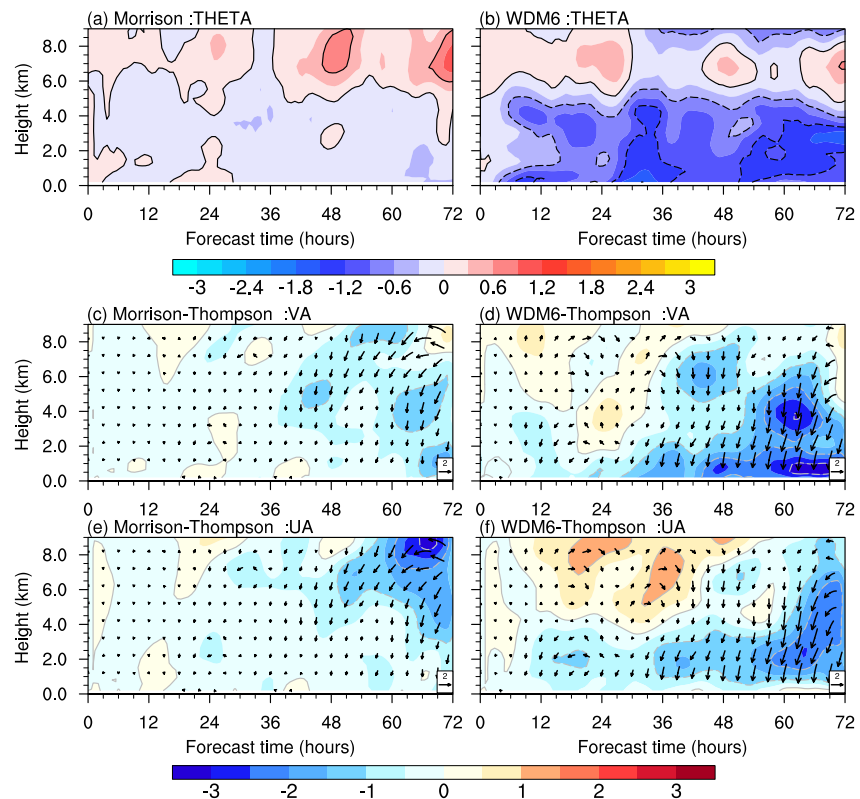
Figure 6. Time–height sections of the difference in (a, b) potential temperature (K), (c, d) meridional wind (VA; m s⁻¹) and (e, f) zonal wind (UA; m s⁻¹) averaged over the area of southerly flow (Figure 2a; red box) between (a, c, e) the Morrison and Thompson experiments and (b, d, e) the WDM6 and Thompson experiments.

Figures 6c–6f show the time–height sections of the difference in the meridional and zonal winds between the Morrison experiment and the WDM6 and Thompson experiments. The Thompson and Morrison experiments generally show less difference in the winds, consistent with the difference in the potential temperature. For example, the difference in the zonal winds between the Morrison and Thompson experiments (Figure 6c) is only about <0.5 m s⁻¹ most of the time. However, in the WDM6 experiment (Figures 6d and 6f), the difference in the meridional and zonal winds in the lower troposphere can reach less than −3 m s⁻¹ after 60 hr. This indicates a weaker southerly flow when less latent heating is produced in the microphysics scheme.

Results show that Thompson and Morrison experiments produce larger stratiform rainfall over southerly flow region (not shown) than that in WDM6 experiment. This is consistent with Morrison et al. (2015), who found that the WDM6 scheme produced larger QRAIN, but lower rainfall over stratiform region compared with the other eight schemes including Thompson and Morrison, which was likely related to the large evaporation rate over stratiform region. This is also consistent with previous studies suggesting high evaporation rates and low stratiform precipitation at the surface (Morrison et al., 2009). In our results, the evaporation rate of QRAIN in WDM6 is maintained at a relatively large value at an altitude of 2–5 km during the first 24 hr of model integration, leading to a decrease in rain mixing ratio, then a decrease in PRACW and eventually an increase in QCLOUD. Therefore, the cloud mixing ratio in the WDM6 experiment is the largest and thus is easier to evaporate, resulting in a significantly lower latent heat than that in the other two experiments.

To investigate the contribution of the variation in the potential temperature in the lower troposphere, Figure 7 shows the 700 hPa wind, potential temperature and geopotential height at 0000 UTC on 20 July 2021, about 6 hr before the maximum rainfall from each scheme. The Thompson experiment (Figure 7b) simulated a strongest southerly wind before the time of maximum rainfall, which is closest to the ERA5 reanalysis data set (Figure 7a), followed by the Morrison experiment (Figure 7c), whereas the WDM6 experiment (Figure 7d) produced a very weak southerly flow consistent with our earlier analysis. The Thompson experiment produced the highest temperature (Figure 7b) but lowest south-north temperature gradient (not shown) over the southerly flow region,
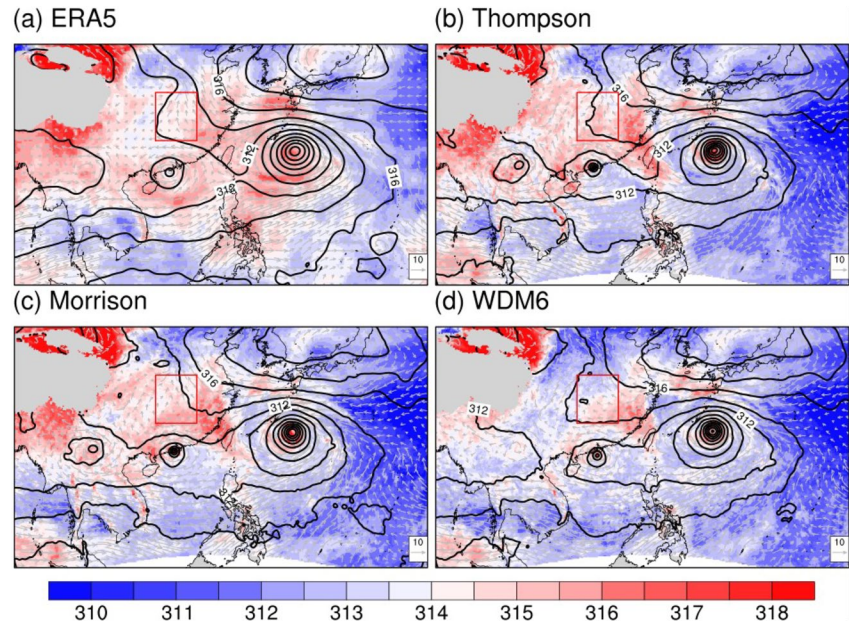
Figure 7. The 700 hPa winds (vectors; m s^{-1}), potential temperature (shading; K) and geopotential height (contours; 10 gpm) for the (a) ERA5, (b) Thompson, (c) Morrison, and (d) WDM6 experiments at 0000 UTC on 20 July 2021.

whereas the WDM6 experiment simulated the lowest temperature (Figure 7d) but highest south-north temperature gradient (not shown), coinciding with the strength of the southerly wind. This could be interpreted from the result that the enhanced temperature led to a smaller gradient in the potential temperature in the south–north direction and then a smaller gradient of geopotential height in the lower troposphere, which, as reported by Potter et al. (2018), favors the maintenance of a southerly flow. This indicates that the changes in potential temperature and south-north temperature gradient with varying latent heating in the microphysics schemes have a crucial role in the differences in the southerly flow in these experiments.

6. Momentum and Thermal Budget

Over area of the southerly flow, it is responsible for resolving the effect of momentum gain and supply of heat fluxes caused by microphysical processes, local dynamics, or ambient weather systems. To isolate different contributions of southerly flow by varying the microphysics schemes, the momentum and thermal budget is calculated from the numerical model. We used inline momentum budget analysis with a similar method as Potter et al. (2018) and Chen et al. (2020) to investigate how the different microphysics schemes contribute to, or inhibit, the strength of the southerly flow. Compared with offline or post-processed momentum budget analysis, inline momentum budget analysis directly extracts all the model budget terms of the budget equation from a prognostic equation during model integration. It is therefore usually the most accurate analysis, with the residual tendency reaching <0.1% of the total tendency. The inline meridional wind momentum equation can be expressed as:

$$\frac{\partial v}{\partial t} = -\nabla \cdot (V v) - f u_{\text{ageo}} + \text{RES} \tag{1}$$

$$\text{VTEN\_TOAL} \quad \text{VTEN\_ADV} \quad \text{VTEN\_AGEO} \quad \text{VTEN\_RES}$$

where the local acceleration of the meridional wind (VTEN_TOAL) equals the sum of advection (VTEN_ADV), $-f u_{\text{ageo}} = \text{VTEN\_COF} + \text{VTEN\_PGF}$ is the ageostrophic force on the meridional winds (VTEN_AGEO), and VTEN_COF $= -f u$ and VTEN_PGF $= -\left(\mu_d a \frac{\partial p}{\partial y} + \left(\frac{a}{a_d} \right) \frac{\partial p}{\partial \eta} \frac{\partial \phi}{\partial y} \right)$ are the Coriolis force and the pressure gradient force, respectively. The forcing term (VTEN_RES) is the meridional wind tendency due to the contribution of horizontal, numerical diffusion, curvature and planetary boundary layer parameterization. The inline meridional
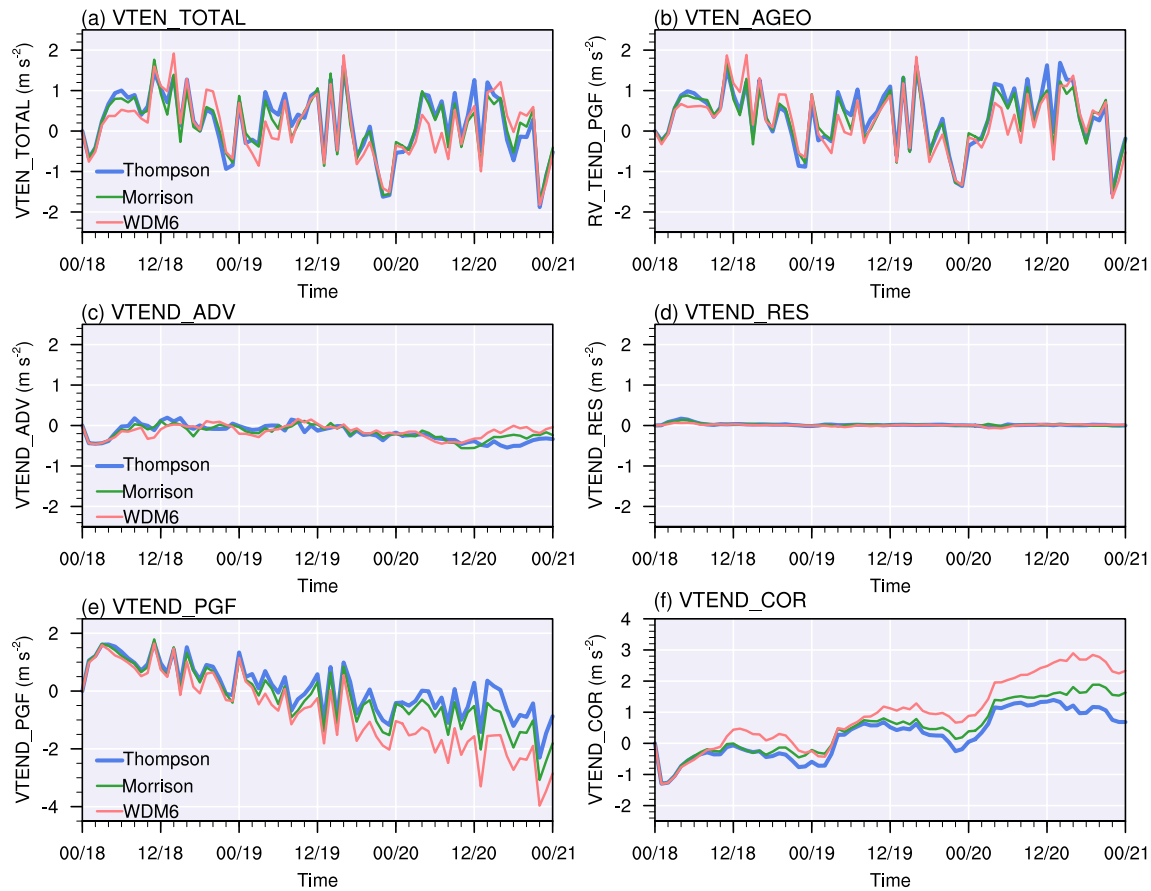
Figure 8. Time series of the (a) total (VTEN_TOTAL), (b) ageostrophic (VTEN_AGEO), (c) advection (VTEN_ADV), (d) residual (VTEN_RES), (e) geostrophic (VTEN_PGF) and (f) Coriolis (VTEN_COR) tendency terms in the meridional wind momentum equation at the 700 hPa averaged over the area of southerly flow (Figure 2a; red box) for the Thompson (blue), Morrison (green) and WDM6 (red) experiments (units: 10^{-4} m s^{-2}).

wind momentum budget is extracted from the model. All the required terms for the momentum budget are directly output or diagnosed from the outermost domain of each experiment.

Figure 8 shows the time series of the four terms in the meridional wind momentum equation at 850 hPa averaged over the southerly flow region. The largest driver of southerly wind acceleration in this region is the Coriolis force acting on the ageostrophic winds (Figure 8b, VTEN_AGEO), followed by advection (Figure 8c, VTEN_ADV), with very low contributions from other forcing terms (Figure 8d, VTEN_RES). There is a clear diurnal cycle in the total tendencies, which is mainly caused by VTEN_AGEO. The evolution of the meridional wind tendencies in each scheme are qualitatively fairly similar, with each scheme showing the diurnal variation in the southerly flow. The most striking difference between the three experiments is the difference in the VTEND_PGF (Figure 8e) and VTEND_COR (Figure 8f) components of VTEND_AGEO. The VTEND_PGF and VTEND_COR terms have negative and positive values, respectively, throughout the entire diurnal cycle and increase gradually throughout the simulation in all experiments.

However, compared with VTEN_AGEO, the differences in the VTEN_PGF and VTEN_COF terms are more evident among the different microphysics schemes and clearly increase with the integration of the model. For example, VTEN_AGEO in the WDM6 experiment, which dominants the difference in the total meridional wind, is smaller than that in the Thompson and Morrison experiments. This could be attributed to the fact that the increase in the negative value of VTEN_PGF in the WDM6 experiment exceeds the increase in the positive value of VTEN_COF. By contrast, the difference in the total tendency (VTEN_TOTAL, Figure 8a) between the WDM6 experiment and the Thompson or Morrison experiments are not as significant as the difference in the VTEN_AGEO as a result of its weaker advection over the southerly flow region. For example, the difference in VEN_TOTAL (Figure 8a) between the WDM6 and Thompson experiments is much lower than that in
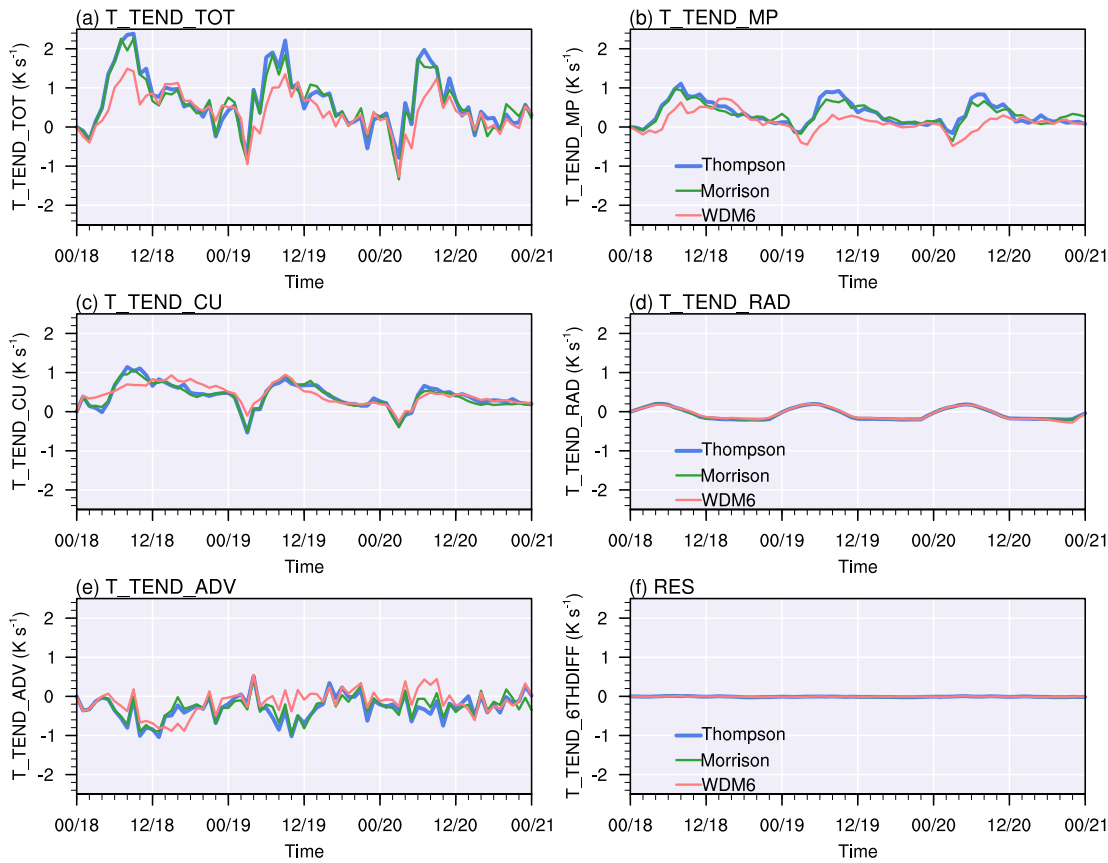
Figure 9. Time series of the (a) total (T_TEND_TOT), (b) microphysics latent heating (T_TEND_MP), (c) cumulus latent heating (T_TEND_CU), (d) radiation (T_TEND_RAD), (e) advection (T_TEND_ADV) and (f) residual (T_TEND_RES) tendency terms in the potential temperature equation at the 700 hPa averaged over the area of southerly flow (Figure 2a; red box) for the Thompson (blue), Morrison (green) and WDM6 (red) experiments (units: 10^{-4} K s^{-1}).

VTEN_AGEO (Figure 8b) from 0000 to 1200 UTC on 20 July 2021. This indicates that the VTEN_AGEO term and the advection term are affected by the microphysics schemes in opposite ways and partially cancel each other out, resulting in a relatively small total tendency.

Similarly, the potential temperature budget over southerly flow region was computed directly extracting all the model budget terms from the potential temperature equation during WRF integration. Each term was output directly during the WRF integration, and then used to calculate the potential temperature budgets, The inline potential temperature equation can be expressed as:

$$\frac{\partial \theta}{\partial t} = -V \cdot \nabla \theta + \frac{\partial \theta}{\partial t}_{MP} + \frac{\partial \theta}{\partial t}_{CU} + \frac{\partial \theta}{\partial t}_{RAD} + \frac{\partial \theta}{\partial t}_{RES} \qquad (2)$$

T_TEND_TOAL   T_TEND_ADV   T_TEND_MP   T_TEND_CU   T_TEND_RAD   T_TEND_RES

where the local acceleration of the potential temperature (T_TEND_TOAL) equals the sum of advection (T_TEND_ADV), microphysics (T_TEND_MP), cumulus parameterization (T_TEND_CU), radiation (T_TEND_RAD) and residual (T_TEND_RES).

In all experiments, the dominance of the microphysics is seen over the southerly flow region (Figure 9). Specifically, the largest component of the potential temperature tendency comes from the microphysics term (Figure 9b). This is followed by cumulus (Figure 9c), and then advection terms (Figure 9e). There are some interesting differences indicated by the three experiments. As would be expected from analyzed above, the largest difference between the three experiments is the microphysics term (T_TEND_MP). The T_TEND_MP difference between Thompson and WDM6 can be as large as over 1×10^{-4} K s^{-1} (Figure 9b). The advection term (T_TEND_ADV) in WDM6 is larger than that in the Thompson and Morrison experiment, suggesting that T_TEND_ADV term

and the T_TEND_MP term are affected by the microphysics schemes in opposite ways and partially cancel each other out, resulting in a relatively small total potential temperature tendency (Figure 9a). Another notable characteristic is that although the magnitude of latent heat due to cumulus parameterization (Figure 9c) is comparable to that due to the microphysical process (Figure 9b), it does not show large discrepancies among the different microphysics schemes. Compared with T_TEND_MP and T_TEND_ADV, the differences in the T_TEND_CU terms are much less evident among the different microphysics schemes and clearly decrease with the integration of the model. A combination of the potential temperature budget for the three microphysics schemes suggests that the differences in potential temperature tendency are mainly caused by differences in latent heat due to microphysics, which is partly canceled by advection term of potential temperature tendency, while latent heat due to cumulus parameterization in three cases do not show large discrepancies.

In summary, the difference in the southerly flow in each experiment appears to be mainly driven by the difference in pressure gradient force. Where does the difference in the pressure gradient force of the southerly flow come from? The difference in latent heating in the different microphysics schemes results in a south–north thermal contrast (Figure 7), which leads to the difference in the pressure gradient over the southerly flow region exceeding the difference in the Coriolis force, which results in a difference in the ageostrophic winds and a stronger southerly flow. The importance of the ageostrophic winds related to thermal forcing along the southerly flow is similar to previous studies of low-level jets (Du et al., 2015; Jiang et al., 2007). However, because the pressure gradient is usually predominantly a result of gradients in the potential temperature, combination of thermal and momentum budget suggests that without sufficient latent heat in the microphysics schemes, the southerly flow is weaker during the Henan extreme rainfall event. Thus, it is clear that, the strengthening of the southerly flow is mainly influenced by the latent heat release from microphysical processes, while the effects of ambient large-scale circulation caused by microphysical processes are relatively small or play a role in weakening the southerly flow.

7. Discussion and Conclusions

An extreme rainfall event took place in Henan from 19 to 21 July 2021, causing a severe disaster and a number of deaths. The first two parts of this study (Xu, Duan, Li, et al., 2022, Xu, Duan, Xu, 2022) showed that the southerly flow, which has a high uncertainty and low predictability, played an important part in determining the areal extent, location and intensity of rainfall over Henan province. This study investigated the effect of microphysical processes on the southerly flow and its indirect effect on the extreme rainfall event. The mesoscale WRF model was used to simulate the southerly flow during the extreme rainfall event with the Thompson, Morrison and WDM6 microphysics parameterizations schemes. The model was able to simulate varying degrees of the distribution and intensity of the extreme rainfall event, but the results showed a strong sensitivity to the parameterization of the microphysics processes. Among the sensitivity tests, the simulated precipitation and southerly flow, which is a key system for extreme rainfall events, clearly varied, with the Thompson scheme simulating the largest precipitation and strongest southerly flow, followed by the Morrison scheme. The WDM6 scheme simulated the smallest precipitation and weakest southerly flow. The results from the microphysics sensitivity experiments confirmed that the coverage and intensity of the extreme rainfall event were highly sensitive to the southerly flow.

However, because the experimental setup only differed in the microphysics scheme, all the differences could be explained by different formulations of the microphysical processes and properties and the corresponding interactions between the microphysics and the related circulations (Xue et al., 2017). Comparisons between the microphysics sensitivity experiments showed that the vertical structures and diurnal cycle of the hydrometeors and latent heating in the Thompson and Morrison experiments were generally fairly similar, except for a stronger QSNOW, lower QICE and slightly stronger latent heating in the Thompson experiment. However, the WDM6 microphysics experiment differed significantly in several ways: the cloud mixing ratio was higher and more persistent, the diurnal cycle was absent after 24 hr of simulation, the rain mixing ratio was significantly lower and latent heating was significantly lower than in the other two experiments. Such differences in the hydrometeors and latent heating during the heavy rainfall event were also found in a previous study with these three microphysics schemes (Bao et al., 2019; Huang et al., 2020).

The indirect effect of different microphysics schemes on the extreme rainfall is understood based on the link between the latent heat and the strength of southerly flow. As the latent heating decreases, a lower value, but stronger gradient, of potential temperature is present over the southerly flow region. The presence of a stronger potential temperature gradient physically leads to a stronger pressure force, a weaker ageostrophic force and then

a weaker total meridional wind tendency. This has implications for increasing the speed of the southerly wind during the Henan extreme rainfall event. For instance, the higher the parameterized latent heating, the stronger and more obvious the southerly flow over south of Henan, with the Thompson experiment producing the strongest southerly flow and the WDM6 experiment simulating a much weaker southerly flow. The result also shows that the Morrison experiment produces slightly weaker latent heating than the Thompson experiment and shows a slightly weaker southerly flow. This could be one of the key reasons why the parameterization of microphysical processes affects the variability of the southerly flow and indirectly influences the distribution and intensity of extreme rainfall. Additional sensitivity experiments with directly reduced or enhanced latent heating of condensation (e.g., 80 or120%) in the Thompson, Morrison and WDM6 experiments will be reported in a future paper, showing both a weaker and stronger simulated southerly flow and indicating that accurate latent heating in microphysics parameterization is not only crucial for the simulation of local rainfall (Bao et al., 2019, 2020; Chen et al., 2022), but also necessary for simulating key synoptic systems near areas of extreme rainfall, which may further improve our understanding of extreme precipitation and its key systems.

The interactions between microphysics and large-scale circulation, especially in an extreme rainfall event which are usually the result of multi-scale interactions, are exceptionally complicated due to the strong feedbacks between dynamics and microphysics (Fan et al., 2012). Thus, the indirect role of microphysical processes on extreme precipitation has been relatively little analyzed in previous studies. Fortunately, we can use ensemble-based analysis to discriminate weather systems that are sensitive (e.g., southerly flow) or insensitive (e.g., intensity of typhoons) to extreme rainfall event (Xu et al., 2022b). In addition, similar to previous studies (Li et al., 2020; Wang, 2009; Zhao et al., 2022), microphysics schemes played an important role in the intensity of the two typhoons for this precipitation event. It is important to examine the impact of typhoon intensity changes on the southerly flow and its indirect effect on the precipitation in Henan region. As in Xu, Duan, Li, et al. (2022), we investigate the influence of the typhoon on the southerly flow by artificially remove the two typhoons. The results show that although the interaction of the binary typhoons and their motion have a significant impact on the southerly flow and precipitation over Henan area, the intensity of the two typhoons does not have a significant impact on the southerly flow and precipitation. Thus, the effect of microphysics schemes on the southerly flow may not be caused by their effect on the intensity of the two typhoons. In this study, the momentum and thermal budget reveal that the southerly flow is mainly due to microphysical processes over southerly flow region, which further confirms the above conclusion.

Finally, we suggest that the variations in the southerly flow as a result of indirect effect of the different microphysics schemes are essential for simulating the sustained intensity of an extreme rainfall event. The simulation of the large-scale circulation, such as the southerly flow, can still be challenging even with state-of-the-art microphysics schemes, especially under conditions of multiscale weather system interactions. Our results highlight that the accurate representation of cloud microphysical processes and their parameterization is essential in numerical models for their key influencing ambient large-scale atmospheric systems. However, this study only focused on the indirect effect of microphysics schemes, whereas direct effect of microphysics schemes on local influencing systems and distribution of extreme rainfall still remains to be examined in future research.

Data Availability Statement

The model outputs presented in this paper are available from Xu (2022). The ERA5 data are available at https://cds.climate.copernicus.eu/cdsapp#!/dataset/reanalysis-era5-pressure-levels?tab=form (CDS, 2022).

References

Bao, J. W., Michelson, S. A., & Grell, E. D. (2019). Microphysical process comparison of three microphysics parameterization schemes in the WRF model for an idealized squall-line case study. *Monthly Weather Review*, *147*(9), 3093–3120. https://doi.org/10.1175/mwr-d-18-0249.1

Bao, X., Wu, L., Zhang, S., Yuan, H., & Wang, H. (2020). A comparison of convective raindrop size distributions in the eyewall and spiral rainbands of Typhoon Lekima (2019). *Geophysical Research Letters*, *47*(23), e2020GL090729. https://doi.org/10.1029/2020GL090729

Bryan, G. H., & Morrison, H. (2012). Sensitivity of a simulated squall line to horizontal resolution and parameterization of microphysics. *Monthly Weather Review*, *140*(1), 202–225. https://doi.org/10.1175/MWR-D-11-00046.1

CDS. (2022). ERA5 [Dataset]. CDS. Retrieved from https://cds.climate.copernicus.eu/cdsapp#!/dataset/reanalysis-era5-pressure-levels?tab=form

Chen, G., Zhao, K., Huang, H., Yang, Z., Lu, Y., & Yang, J. (2021). Evaluating simulated raindrop size distributions and ice microphysical processes with polarimetric radar observations in a Meiyu front event over eastern China. *Journal of Geophysical Research: Atmospheres*, *126*(22), e2020JD034511. https://doi.org/10.1029/2020JD034511

Chen, G., Zhao, K., Lu, Y., Zheng, Y., Xue, M., Tan, Z.-M., et al. (2022). Variability of microphysical characteristics in the "21·7" Henan extremely heavy rainfall event. *Science China Earth Sciences*, *65*(10), 1861–1878. https://doi.org/10.1007/s11430-022-9972-9

Chen, T. C., Yau, M. K., & Kirshbaum, D. J. (2020). Towards the closure of momentum budget analyses in the WRF (v3.8.1) model. *Geoscientific Model Development*, *13*(3), 1737–1761. https://doi.org/10.5194/gmd-13-1737-2020

Dowell, D. C., Alexander, C. R., James, E. P., Weygandt, S. S., Benjamin, S. G., Manikin, G. S., et al. (2022). The High-Resolution Rapid Refresh (HRRR): An hourly updating convection-allowing forecast model. Part I: Motivation and system description. *Weather and Forecasting*, *37*(8), 1371–1395. https://doi.org/10.1175/waf-d-21-0151.1

Du, Y., Chen, Y.-L., & Zhang, Q. (2015). Numerical simulations of the boundary layer jet off the southeastern coast of China. *Monthly Weather Review*, *143*(4), 1212–1231. https://doi.org/10.1175/mwr-d-14-00348.1

Falk, N. M., Igel, A. L., & Igel, M. R. (2019). The relative impact of ice fall speeds and microphysics parameterization complexity on supercell evolution. *Monthly Weather Review*, *147*(7), 2403–2415. https://doi.org/10.1175/mwr-d-18-0417.1

Fan, J., Rosenfeld, D., Ding, Y., Leung, L. R., & Li, Z. (2012). Potential aerosol indirect effects on atmospheric circulation and radiative forcing through deep convection. *Geophysical Research Letters*, *39*(9). https://doi.org/10.1029/2012GL051851

Ferrier, B. S., Tao, W.-K., & Simpson, J. (1995). A double-moment multiple-phase four-class bulk ice scheme. Part II: Simulations of convective storms in different large-scale environments and comparisons with other bulk parameterizations. *Journal of the Atmospheric Sciences*, *52*(8), 1001–1033. https://doi.org/10.1175/1520-0469(1995)052<1001:admmpf>2.0.co;2

Fu, S.-M., Zhang, Y.-C., Wang, H.-J., Tang, H., Li, W.-L., & Sun, J.-H. (2022). On the evolution of a long-lived mesoscale convective vortex that acted as a crucial condition for the extremely strong hourly precipitation in Zhengzhou. *Journal of Geophysical Research: Atmospheres*, *127*(11), e2021JD036233. https://doi.org/10.1029/2021JD036233

Gao, W., Xue, L., Liu, L., Lu, C., Yun, Y., & Zhou, W. (2021). A study of the fraction of warm rain in a pre-summer rainfall event over South China. *Atmospheric Research*, *262*, 105792. https://doi.org/10.1016/j.atmosres.2021.105792

Halder, M., Hazra, A., Mukhopadhyay, P., & Siingh, D. (2015). Effect of the better representation of the cloud ice-nucleation in WRF microphysics schemes: A case study of a severe storm in India. *Atmospheric Research*, *154*, 155–174. https://doi.org/10.1016/j.atmosres.2014.10.022

Hong, S.-Y., & Lim, J.-O. J. (2006). The WRF single-moment 6-class microphysics scheme (WSM6). *Asia Pacific Journal of Atmospheric Sciences*, *42*(2), 129–151. Retrieved from https://www2.mmm.ucar.edu/wrf/users/workshops/WS2006/abstracts/PSession05/P5_4_Hong.pdf

Huang, Y., Wang, Y., Xue, L., Wei, X., Zhang, L., & Li, H. (2020). Comparison of three microphysics parameterization schemes in the WRF model for an extreme rainfall event in the coastal metropolitan City of Guangzhou, China. *Atmospheric Research*, *240*, 104939. https://doi.org/10.1016/j.atmosres.2020.104939

Jiang, X., Lau, N.-C., Held, I. M., & Ploshay, J. J. (2007). Mechanisms of the great plains low-level jet as simulated in an AGCM. *Journal of the Atmospheric Sciences*, *64*(2), 532–547. https://doi.org/10.1175/jas3847.1

Khain, A. P., Beheng, K. D., Heymsfield, A., Korolev, A., Krichak, S. O., Levin, Z., et al. (2015). Representation of microphysical processes in cloud-resolving models: Spectral (bin) microphysics versus bulk parameterization. *Reviews of Geophysics*, *53*(2), 247–322. https://doi.org/10.1002/2014RG000468

Kreidenweis, S. M., Petters, M., & Lohmann, U. (2019). 100 years of progress in cloud physics, aerosols, and aerosol chemistry research. *Meteorological Monographs*, *59*, 11.11–11.72. https://doi.org/10.1175/amsmonographs-d-18-0024.1

Lei, H., Guo, J., Chen, D., & Yang, J. (2020). Systematic bias in the prediction of warm-rain hydrometeors in the WDM6 microphysics scheme and modifications. *Journal of Geophysical Research: Atmospheres*, *125*(4), e2019JD030756. https://doi.org/10.1029/2019JD030756

Li, J., Ding, C., Li, F., & Chen, Y. (2020). Effects of single- and double-moment microphysics schemes on the intensity of super typhoon Sarika (2016). *Atmospheric Research*, *238*, 104894. https://doi.org/10.1016/j.atmosres.2020.104894

Lim, K. S. S., & Hong, S. Y. (2010). Development of an effective double-moment cloud microphysics scheme with prognostic cloud condensation nuclei (CCN) for weather and climate models. *Monthly Weather Review*, *138*(138), 1587–1612. https://doi.org/10.1175/2009mwr2968.1

Luo, L., Xue, M., Zhu, K., & Zhou, B. (2018). Explicit prediction of hail in a long-lasting multicellular convective system in eastern China using multimoment microphysics schemes. *Journal of the Atmospheric Sciences*, *75*(9), 3115–3137. https://doi.org/10.1175/jas-d-17-0302.1

Morrison, H., & Milbrandt, J. (2011). Comparison of two-moment bulk microphysics schemes in idealized supercell thunderstorm simulations. *Monthly Weather Review*, *139*(4), 1103–1130. https://doi.org/10.1175/2010mwr3433.1

Morrison, H., Milbrandt, J. A., Bryan, G. H., Ikeda, K., Tessendorf, S. A., & Thompson, G. (2015). Parameterization of cloud microphysics based on the prediction of bulk ice particle properties. Part II: Case study comparisons with observations and other schemes. *Journal of the Atmospheric Sciences*, *72*(1), 312–339. https://doi.org/10.1175/jas-d-14-0066.1

Morrison, H., Thompson, G., & Tatarskii, V. (2009). Impact of cloud microphysics on the development of trailing stratiform precipitation in a simulated squall line: Comparison of one- and two-moment schemes. *Monthly Weather Review*, *137*(3), 991–1007. https://doi.org/10.1175/2008mwr2556.1

Morrison, H., van Lier-Walqui, M., Fridlind, A. M., Grabowski, W. W., Harrington, J. Y., Hoose, C., et al. (2020). Confronting the challenge of modeling cloud and precipitation microphysics. *Journal of Advances in Modeling Earth Systems*, *12*(8), e2019MS001689. https://doi.org/10.1029/2019MS001689

Nakanishi, M., & Niino, H. (2006). An improved Mellor–Yamada Level-3 model: Its numerical stability and application to a regional prediction of advection fog. *Boundary-Layer Meteorology*, *119*(2), 397–407. https://doi.org/10.1007/s10546-005-9030-8

Nie, Y., & Sun, J. (2022). Moisture sources and transport for extreme precipitation over Henan in July 2021. *Geophysical Research Letters*, *49*(4), e2021GL097446. https://doi.org/10.1029/2021GL097446

Olson, J. B., Kenyon, J. S., Angevine, W. A., Brown, J. M., Pagowski, M., & Sušelj, K. (2019). A description of the MYNN-EDMF scheme and the coupling to other components in WRF–ARW (Technical Memorandum). Retrieved from https://repository.library.noaa.gov/view/noaa/19837

Potter, E. R., Orr, A., Willis, I. C., Bannister, D., & Salerno, F. (2018). Dynamical drivers of the local wind regime in a Himalayan valley. *Journal of Geophysical Research: Atmospheres*, *123*(23), 13186–13202. https://doi.org/10.1029/2018JD029427

Siebesma, A. P., Soares, P. M. M., & Teixeira, J. (2007). A combined Eddy-Diffusivity Mass-Flux approach for the convective boundary layer. *Journal of the Atmospheric Sciences*, *64*(4), 1230–1248. https://doi.org/10.1175/jas3888.1

Tapiador, F. J., Sánchez, J.-L., & García-Ortega, E. (2019). Empirical values and assumptions in the microphysics of numerical models. *Atmospheric Research*, *215*, 214–238. https://doi.org/10.1016/j.atmosres.2018.09.010

Thomas, B., Viswanadhapalli, Y., Srinivas, C. V., Dasari, H. P., Attada, R., & Langodan, S. (2021). Cloud resolving simulation of extremely heavy rainfall event over Kerala in August 2018—Sensitivity to microphysics and aerosol feedback. *Atmospheric Research*, *258*, 105613. https://doi.org/10.1016/j.atmosres.2021.105613

Thompson, G., & Eidhammer, T. (2014). A study of aerosol impacts on clouds and precipitation development in a large winter cyclone. *Journal of the Atmospheric Sciences*, *71*(10), 3636–3658. https://doi.org/10.1175/jas-d-13-0305.1

Wang, J., Fan, J., Feng, Z., Zhang, K., Roesler, E., Hillman, B., et al. (2021). Impact of a new cloud microphysics parameterization on the simulations of mesoscale convective systems in E3SM. *Journal of Advances in Modeling Earth Systems*, *13*(11), e2021MS002628. https://doi.org/10.1029/2021MS002628

Wang, Y. (2009). How do outer spiral rainbands affect tropical cyclone structure and intensity? *Journal of the Atmospheric Sciences*, *66*(5), 1250–1273. https://doi.org/10.1175/2008JAS2737.1

Wang, Y., Wang, Y., & Fudeyasu, H. (2009). The role of typhoon Songda (2004) in producing distantly located heavy rainfall in Japan. *Monthly Weather Review*, *137*(11), 3699–3716.

Xu, H. (2022). Data sets associated with "Indirect effects of binary typhoons on an extreme rainfall event in Henan province, China from July 19 to 21, 2021. Part 3: Sensitivities to microphysics schemes" [Dataset]. Zenodo. https://doi.org/10.5281/zenodo.7402401

Xu, H., Duan, Y., Li, Y., & Wang, H. (2022). Indirect effects of binary typhoons on an extreme rainfall event in Henan province, China from 19 to 21 july 2021: 2. Numerical study. *Journal of Geophysical Research: Atmospheres*, *127*(17), e2021JD036083. https://doi.org/10.1029/2021JD036083

Xu, H., Duan, Y., & Xu, X. (2022). Indirect effects of binary typhoons on an extreme rainfall event in Henan province, China from 19 to 21 july 2021: 1. Ensemble-Based analysis. *Journal of Geophysical Research: Atmospheres*, *127*(10), e2021JD036265. https://doi.org/10.1029/2021JD036265

Xue, L., Fan, J., Lebo, Z. J., Wu, W., Morrison, H., Grabowski, W. W., et al. (2017). Idealized simulations of a squall line from the MC3E field campaign applying three bin microphysics schemes: Dynamic and thermodynamic structure. *Monthly Weather Review*, *145*(12), 4789–4812. https://doi.org/10.1175/mwr-d-16-0385.1

Yin, J., Gu, H., Liang, X., Yu, M., Sun, J., Xie, Y., et al. (2022). A possible dynamic mechanism for rapid production of the extreme hourly rainfall in Zhengzhou city on 20 July 2021. *Journal of Meteorological Research*, *36*(1), 6–25.

Zhang, X. (2019). Multiscale characteristics of different-source perturbations and their interactions for convection-permitting ensemble forecasting during SCMREX. *Monthly Weather Review*, *147*(1), 291–310. https://doi.org/10.1175/mwr-d-18-0218.1

Zhao, D., Gao, W., Xu, H., Yu, Y., & Chen, L. (2022). A modeling study of cloud physical properties of extreme and non-extreme precipitation in landfalling typhoons over China. *Atmospheric Research*, *277*, 106311. https://doi.org/10.1016/j.atmosres.2022.106311

Zhao, D., Yu, Y., Yin, J., & Xu, H. (2020). Effects of microphysical latent heating on the rapid intensification of typhoon Hato (2017). *Journal of Meteorological Research*, *34*(2), 368–386. https://doi.org/10.1007/s13351-020-9076-z

Zhou, L., Lin, S.-J., Chen, J.-H., Harris, L. M., Chen, X., & Rees, S. L. (2019). Toward convective-scale prediction within the next generation global prediction system. *Bulletin of the American Meteorological Society*, *100*(7), 1225–1243. https://doi.org/10.1175/bams-d-17-0246.1